High-temperature multigap superconductivity in two-dimensional metal borides

Cem Sevik,[1,2,*,†] Jonas Bekaert,[1,*,‡] Mikhail Petrov,[1] and Milorad V. Milošević[1,§]
[1]*Department of Physics & NANOlab Center of Excellence, University of Antwerp, Groenenborgerlaan 171, B-2020 Antwerp, Belgium*
[2]*Department of Mechanical Engineering, Faculty of Engineering, Eskisehir Technical University, 26555 Eskisehir, Turkey*

(Received 5 December 2021; revised 31 January 2022; accepted 14 February 2022; published 28 February 2022)

Using first-principles calculations in combination with the Eliashberg formalism, we systematically investigated phonon-mediated superconductivity in two-dimensional (2D) metal-boride crystals, consisting of a boron honeycomb network doped by diverse metal elements. Such 2D metal-boride compounds, named MBenes, are chemically exfoliable from single-crystalline layered ternary borides. First we identified the MBene layers with potential for superconductivity via isotropic Eliashberg calculations, considering a wide range of metal elements, with a focus on alkaline earth and transition metals. Subsequently, we performed a detailed analysis of the prominent superconducting MBenes by solving the anisotropic Eliashberg equations. The obtained high critical temperatures (up to 72 K), as well as the rich multigap superconducting behavior, recommend these crystals for further use in multifunctional 2D heterostructures and superconducting device applications.

DOI: 10.1103/PhysRevMaterials.6.024803

I. INTRODUCTION

The potential of two-dimensional (2D) materials in terms of future technological applications is well established [1–3], as demonstrated, for example, through both theoretical and experimental studies with regard to transistors [4,5], energy harvesters [6–9], and sensors [10–12]. Recently, with the successful fabrication of 2D metallic materials such as In [13], Pb [14], $NbSe_2$ [15,16], FeSe [17], MgB_2 [18], Mo_2C [19], Nb_2C [20], doped graphene [21–23], and twisted bilayer graphene [24], superconductivity has been added to the range of properties yielding possible applications. However, taking advantage of that potential requires a detailed investigation and understanding of the origins and behavior of the superconductivity in these 2D systems to ensure reproducibly robust superconducting behavior up to sufficiently high temperatures.

One of the well-known material families to examine the behavior of superconductivity at the 3D-to-2D transition are the layered hexagonal metal borides (MB_2) with *P6/mmm* space-group symmetry. Among them, bulk MgB_2 has been extensively studied over the past two decades and is still the electron-phonon (*e-ph*)-mediated superconductor with the highest experimentally realized superconducting transition temperature at ambient pressure to date ($T_c = 39$ K) [25]. The experimental demonstration of two-gap superconductivity in this material has led to an immensely intensified interest in this area and a paradigm shift in superconductivity research. On that wave, superconductivity has also been experimentally validated in identical bulk crystals of ZrB_2 [26], NbB_2 [27], and TaB_2 [28]. Furthermore, an elevated T_c of 48 K has been predicted for bulk CaB_2, based on anisotropic Eliashberg calculations [29].

When thinned down to monolayer thicknesses, MgB_2 was demonstrated to harbor a very strong influence of the surface states [30], leading to three-gap superconductivity with $T_c = 20$ K in the monolayer limit [31], strongly changing with every added monolayer, up to several nanometers thickness. Moreover, a strong increase in the T_c of 2D MgB_2 (to over 100 K) with hydrogenation and tensile strain have been revealed [32]. With the same crystal structure, single-layer AlB_2 has been predicted as a two-gap superconductor with $T_c = 26.5$ K [33,34], surpassing single-layer MgB_2, although its bulk form is not superconducting at all. Last but not least, one is also interested in possible growth of MB_4 2D crystals, with the metal layer sandwiched between two boron honeycomb networks. In that respect, Li-, Be-, Mg-, Al-, and Ga-based MB_4 structures have been recently predicted to possess a multigap superconducting nature, all with T_c above 30 K [34]. All together, the research to date clearly indicates the potential of layered metal-boride systems to realize 2D superconductivity.

It is therefore instructive to have a comparative analysis of different possible 2D metal borides. When considering the experimentally grown bulk metal borides with the same crystal symmetry [35], one notices that *e-ph* mediated superconducting properties of Ca-, Sc-, Ti-, Zr-, Hf-, V-, Nb-, Ta-, Cr-, Mo-, W- and Re-based 2D MBenes have not been explored. As a matter of fact, a recent first-principles study indicated the feasibility of synthesizing the layered MAB (layered ternary transition metal borides, where M is a transition metal, A is a group-13 or group-14 element, and B is boron) bulk crystals of hexagonal metal borides of Sc, Ti, Zr, Hf, V, Nb, Ta, Mo, and W, starting from the MAB bulk crystals [36], from which 2D MBenes are exfoliable

*These authors contributed equally to this work.
†csevik@eskisehir.edu.tr
‡jonas.bekaert@uantwerpen.be
§milorad.milosevic@uantwerpen.be

(with name derived analogously to MXenes obtained from MAX (layered ternary transition metal carbides and nitrides, where M is an early transition metal, A is a group-13 or group-14 element, and X is C or N) bulk phases [37]). Note, however, that layer-by-layer exfoliation of these materials is not as straightforward as for graphene, due to the strong interaction between the metal and the boron layers. Therefore, one must consider several possible 2D formations, including MB_4 (a metal layer sandwiched between two honeycomb B lattices, where the metal atoms are placed in the centers of honeycombs), MB_2 (a B layer in a honeycomb lattice and a layer of metal atoms sitting above the centers of honeycombs), and M_2B_2 (a B layer in a honeycomb lattice sandwiched between two layers of metal atoms sitting above/below the centers of honeycombs). Therefore, in this paper we comprehensively investigated superconductivity in different exfoliable MBene structures (derived from layered bulk MAB and MB_2 structures), with particular attention to Ca-, Sc-, Ti-, Zr-, Hf-, V-, Nb-, Ta-, Cr-, Mo-, W-, and Re-based ones, in comparison to the previously studied Be-, Mg-, and Al-based di- and tetraborides. Following the selection of the most prominent superconducting MBenes, we detail their anisotropic superconducting properties, origin of their multiple superconducting gaps, and their high critical temperature.

The organization of the paper is as follows. First, we describe the used computational approaches and adopted parameters for the calculations. Then, we present detailed isotropic Eliashberg theory results for all the considered materials. These results are then used to select the materials that potentially possess good superconducting properties. Finally, we summarize the results of detailed anisotropic Eliashberg calculations for the selected materials. Extensive additional results for electronic, vibrational, and superconducting properties are made available in the Supplemental Material [38].

II. COMPUTATIONAL METHODS AND DETAILS

The considered metal-boride layers, 45 in total, were investigated through density functional theory, as implemented within the ABINIT [39,40] code, using the Perdew-Burke-Ernzerhof (PBE) functional. Relativistic pseudopotentials from the PseudoDojo project [41] were used where we could include spin-orbit coupling (SOC) if necessary. Namely, we calculated electronic structures both without and with SOC for all compounds, and if significant differences were found in the states responsible for collective electron behavior, i.e., those near the Fermi level (E_F), we proceeded with the inclusion of SOC in further calculations. Within the used pseudopotentials $10 + N$ valence electrons were used for metal elements of group N, except for Be (four valence electrons), and three valence electrons were taken into account for B. An energy cutoff value of 60 Ha for the plane-wave basis and a dense $36 \times 36 \times 1$ k-point grid were used to achieve high accuracy. The structures, with at least 16 Å of vacuum, were relaxed so forces on each atom were below 1 meV/Å. Subsequently, to calculate phonons and the electron-phonon coupling (EPC), we employed density functional perturbation theory (DFPT), also within ABINIT [42], using the same electronic k-point grid and a $12 \times 12 \times 1$ phononic q-point grid. For the calculations of the superconducting state, we used isotropic Eliashberg theory, a quantitatively accurate extension to the Bardeen-Cooper-Schrieffer theory for phonon-mediated superconductivity [43–45]. We evaluated the superconducting T_c using the Allen-Dynes formula [46–48], and a screened Coulomb repulsion of $\mu^* = 0.13$—a standard value for transition metal-based compounds [49]. In addition, the cohesive energy values of the structures (per atom) were calculated using the following formula:

$$E_{\text{coh}} = \frac{nE_M + lE_B - E_{M_nB_l}}{n + l}, \tag{1}$$

where E_M and E_B are the total energies of the isolated metal and B atoms, respectively, and $E_{M_nB_l}$ is the total energy of the corresponding 2D MBene. In view of this expression, materials with more positive E_{coh} indicate a higher chemical stability.

Subsequently, for the materials predicted to possess high T_c values, a self-consistent solution of the fully anisotropic Migdal-Eliashberg equation was obtained through the ELECTRON-PHONON WANNIER (EPW) code [45,50,51]. For that part, first-principles calculations were performed with the QUANTUM ESPRESSO package [52], using the same PBE pseudopotentials. The cutoffs for the plane-wave basis and charge density were set to 100 Ry and 400 Ry, respectively. The k-point mesh for the integration in wave-vector space was set to $24 \times 24 \times 1$, and electronic smearing was performed within the Methfessel-Paxton scheme [53]. With these parameters, the structures were fully optimized until the Hellman-Feynman forces on each atom were below 10^{-4} Ry/bohr. The subsequent dynamical properties were calculated based on the DFPT as implemented in QUANTUM ESPRESSO package [54], using a q-mesh of $12 \times 12 \times 1$. The maximally localized Wannier functions [55,56] required in the EPW calculations were interpolated by using an unshifted Brillouin-zone k-mesh of $12 \times 12 \times 1$. The solution of the anisotropic Migdal-Eliashberg equations was computed with interpolated k- and q-point grids of $240 \times 240 \times 1$ and $120 \times 120 \times 1$, which are sufficiently dense to guarantee convergence of the superconducting gaps. The cutoff for the fermion Matsubara frequencies $\omega_j = (2j + 1)\pi T$ was set to 0.5 eV and μ^* was the same as in the isotropic calculations (0.13).

III. RESULTS

As mentioned above, we considered three different exfoliable MBene structures, namely, MB_4 (consisting of a metal layer sandwiched between two B layers), M_2B_2 (consisting of a B layer sandwiched between two M layers), and MB_2 (consisting of one B and one M layer). As the first step, the equilibrium lattice structures of these metal-boride layers, schematically represented in Fig. 1, were predicted and compared with the available data. The calculated in-plane lattice constants (listed in the Supplemental Material) are in good agreement both with available experimental values for bulk structures [18,26,35,57] and with calculated values for the same single-layer crystals available in the literature [30,33,58]. The phonon dispersions presented in the Supplemental Material clearly point out the dynamical stability of all the considered crystals with the exception of BeB_2, TiB_4,

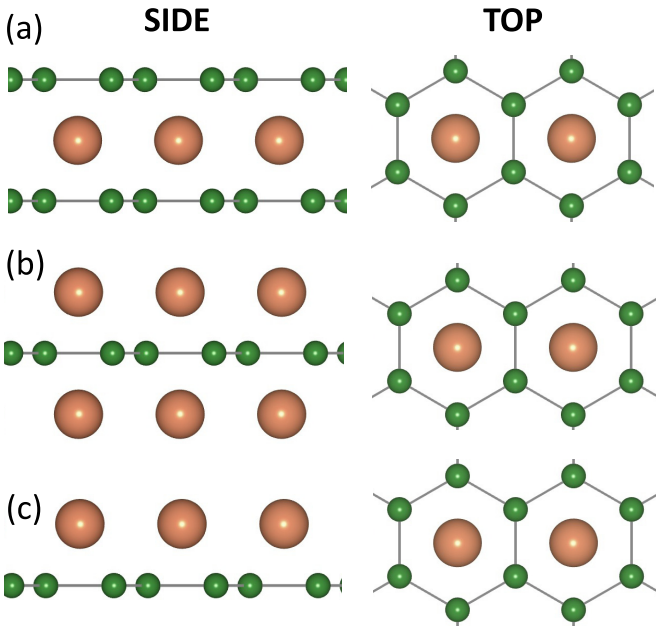

FIG. 1. Crystal structures of the considered (a) MB_4, (b) M_2B_2, and (c) MB_2. Here, green and orange spheres represent the boron and metal atom, respectively.

ZrB_4, HfB_4, and ReB_4. Furthermore, the cohesive energy value, a widely accepted parameter used to evaluate the chemical stability of crystals [see Eq. (1)], was evaluated for each monolayer. Promisingly, the corresponding values presented in Table I are comparable with the ones obtained for several experimentally realized monolayers, e.g., graphene (7.46 eV per atom), silicene (3.71 eV per atom), and black phosphorene (2.57 eV per atom). Based on these results, MB_4 is identified as the configuration with the highest cohesive energy per atom for Be-, Mg-, Ca-, Sc-, V-, Cr-, Mo-, and Al-based monolayers, while M_2B_2 is the favored structure for the Ti-, Zr-, Hf-, Nb-, Ta-, W-, and Re-based ones.

Subsequently, we investigated the electronic properties of each material and found nearly all the structures to be metallic. However, TiB_2 has a graphenelike band structure possessing a Dirac cone at the Fermi level as previously reported [58]. Also, BeB_2, ZrB_2, HfB_2, CrB_4, MoB_4, and WB_4 were predicted to possess a very low electronic density of states at the Fermi level due to single or multiple Dirac cones close to the Fermi level, which is a clear obstacle for the formation of the superconducting state. As a result of this preliminary analysis, we eliminated these materials and computed the superconducting properties for the other candidates. Our isotropic Eliashberg theory calculations show that five MB_4, ten MB_2, and two M_2B_2 crystals from Table II possess a sizable superconducting T_c. Among these materials, BeB_4, MgB_4, AlB_4, AlB_2, and MgB_2 have been previously investigated [33,34]. Indeed, our results for the superconducting transition temperature T_c are comparable with the ones obtained in these references (where anisotropic Eliashberg theory was used). Also, the T_c obtained for MgB_4 in this paper (22.2 K), is in very good agreement with the one calculated by Liao *et al.* in Ref. [59] (23.2 K).

TABLE I. Calculated cohesive energy, E_{coh}, of the considered monolayer metal-boride structures.

	E_{coh} (eV/atom)				E_{coh} (eV/atom)		
Metal	MB_4	MB_2	M_2B_2	Metal	MB_4	MB_2	M_2B_2
Be	5.32	5.15	4.51	V	6.04	5.58	5.76
Mg	4.86	4.20	3.75	Nb	6.40	6.14	6.68
Ca	4.83	4.17	4.00	Ta	6.64	6.48	7.16
Sc	5.70	5.33	5.56	Cr	5.60	4.94	4.75
Ti	6.38	6.22	6.77	Mo	6.15	5.73	5.95
Zr	6.38	6.29	7.04	W	6.55	6.35	6.75
Hf	6.41	6.28	6.99	Re	6.27	6.10	6.30
Al	5.27	4.73	4.42				

TABLE II. Calculated lattice constant (a), electronic DOS at the Fermi level (N_F), average Fermi velocity (v_F), *e-ph* coupling (λ), logarithmic average of phonon frequencies (ω_{ln}), and Allen-Dynes superconducting transition temperature (T_c) for all considered MBenes.

Metal	a (Å)	N_F ($eV^{-1}atom^{-1}$)	v_F ($10^6 ms^{-1}$)	λ	ω_{ln} (K)	T_c (K)
			MB_4 monolayers			
Be	2.968	0.111	0.466	1.212	371	29.9
Mg	3.007	0.143	0.678	0.808	573	22.2
Ca	3.075	0.267	0.484	1.196	457	36.1
Sc	3.080	0.220	0.324	0.714	371	10.4
Al	2.991	0.199	0.527	0.911	615	30.9
			MB_2 monolayers			
Mg	3.044	0.324	0.606	0.65	555	11.6
Ca	3.220	0.841	0.277	1.67	360	41.6
Sc	3.176	1.111	0.201	1.06	308	20.4
Zr	3.152	0.485	0.211	0.67	125	2.9
V	3.064	0.887	0.219	2.70	50	8.3
Nb	2.997	1.145	0.191	2.23	245	35.5
Ta	3.002	0.718	0.318	0.75	220	7.1
Cr	3.128	1.101	0.311	1.68	36	4.5
Re	2.882	0.417	0.408	0.55	215	2.4
Al	2.981	0.395	0.680	1.40	98	9.8
			M_2B_2 monolayers			
Mg	3.104	0.187	0.665	0.486	498	3.2
Re	2.916	0.321	0.317	1.088	81	5.5

Having evaluated the results obtained within the isotropic limit, we focus further on several materials with the most promising superconducting properties. Among the considered MBenes, CaB_4, CaB_2, NbB_2, and ScB_2 with high T_c values of 36.1, 41.6, 35.5, and 20.4 K were identified as the most prominent superconductors. Also, the group-5-based compounds VB_2, NbB_2, TaB_2 are worthy of further investigation. The strong hybridization between B $2p$ and transition metal d states should be taken into consideration for VB_2, NbB_2, TaB_2, and ScB_2. Zhang *et al.* investigated how d orbitals stemming from Nb split into (d_{xy}, $d_{x^2-y^2}$), (d_{xz}, d_{yz}), and (d_{z^2}) around the Fermi level in NbB_2 [58]. Therefore, we performed fully anisotropic Eliashberg calculations for CaB_2, CaB_4, VB_2, NbB_2, TaB_2, and ScB_2 to fully characterize the origin and behavior of superconductivity in MBenes.

Calcium borides—CaB_2 and CaB_4—have proven to be the most prominent superconductors among the considered structures. The Fermi surface of CaB_2, shown in Fig. 3(c),

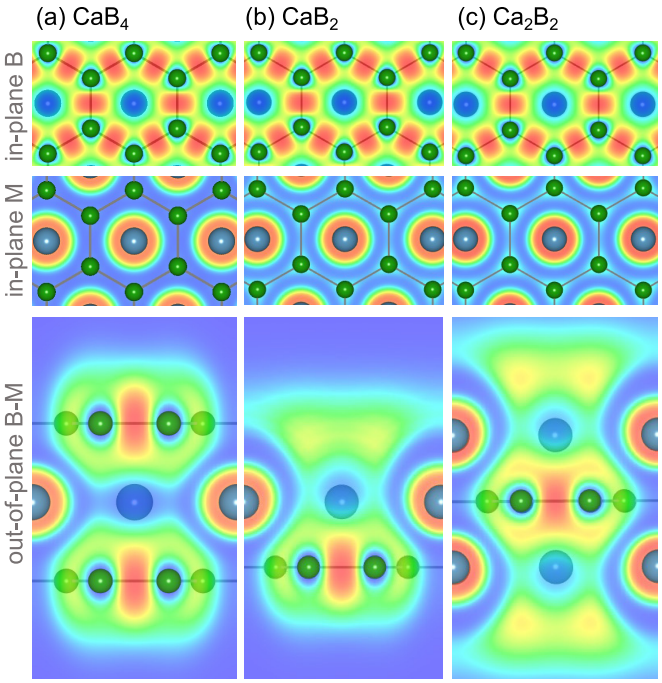

FIG. 2. Calculated electron localization function (ELF) of the considered (a) CaB_4, (b) CaB_2, and (c) Ca_2B_2 crystals. Here, the color spectrum ranging from blue to red corresponds to the electron pair probability from low to high.

closely resembles that of MgB_2, consisting of two σ bands, a π band and a surface band. Both σ (consisting of $s + p_{x,y}$) and π (consisting of p_z) electronic states are localized in the layer of boron atoms while the surface state is mainly localized on top of the Ca layer facing vacuum. As in MgB_2 (monolayer as well as bulk) [60], the B–B bonds in Ca-based MBenes are mainly of covalent nature, as can be observed from their electron localization functions, shown in Fig. 2 (calculated in ABINIT). While the σ Fermi sheets are located around the Γ point, the π orbitals contribute Fermi sheets centered around the K point, hosting distinct superconducting properties. Moreover, these π sheets are larger in CaB_2 compared to MgB_2, extending to the vicinity of the M point. As a result, the density of states at Fermi level (N_F) of monolayer CaB_2 is more than twice that of monolayer MgB_2 (see Table II), clearly enhancing its superconductivity. The Fermi surface of CaB_4, shown in Fig. 3(f), for the most part retains the same features as CaB_2, with one exception. Since the calcium layer in CaB_4 is fully encapsulated between two boron layers, the surface state is suppressed. When comparing MgB_4 with CaB_4, N_F is almost two times higher in the latter, akin to the case of their MB_2 counterparts.

The phonon band structures of the calcium borides, as shown in Figs. 3(a) and 3(d), are quite different. In CaB_2, acoustic and optical phonon modes are separated by an energy gap, which gets completely suppressed in CaB_4, notwithstanding the similarity of the corresponding atomic displacements in both compounds. These different phonon dispersions lead to different EPC in the two compounds, as shown in Figs. 3(a) and 3(d). As can be seen from the Eliashberg function α^2F of CaB_2, acoustic and optical phonon modes contribute almost equally to the total EPC of 1.59, whereas for CaB_4, due to the absence of the gap in the phonon dispersion, one cannot make a clear distinction in the Eliashberg function between acoustic and optical phonon modes. The total EPC of the calcium tetraboride is 1.43, which is slightly lower than in the diboride. As in the case of MgB_2 [31], in both calcium boride compounds a significant part of the total EPC comes from two in-plane optical phonon modes (with mode indices 4 and 5), belonging to the E_2 class. The EPC due to these modes peaks at Γ [Fig. 3(a)], where $\lambda_{\Gamma,4} = \lambda_{\Gamma,5} = 5.9$. Likewise, the main coupling modes in CaB_4 belong to the E_{2g} class (mode indices 10 and 11), which at Γ amount to $\lambda_{\Gamma,10} = \lambda_{\Gamma,11} = 1.9$. λ_{mode} for different groups of phonon modes [Fig. 3(a) and 3(d)] also reveals differences in the character of the EPC when comparing CaB_2 and CaB_4. While highly coupling phonon states in the former are fairly localized around the Γ point, there is also a sizable contribution from other parts of the Brillouin zone (particularly along Γ-M) in the latter.

Based on our fully anisotropic Eliashberg calculations, we can analyze how different electronic states on the Fermi surface contribute to superconductivity, through the anisotropic gap spectrum $\Delta(\mathbf{k})$. At a temperature of 5 K, the largest Δ values, reaching as high as 17.4 meV in CaB_2, stem from the B-σ states, while gaps of the B-π and surface states are highly anisotropic, ranging from 1.7 to 7.5 meV [Fig. 3(c)]. The superconducting gap distribution for calcium diboride, as shown in Fig. 3(b), shows two distinct superconducting gaps: the strongest σ-state gap, and a highly anisotropic gap which is a hybrid formed by the π and the surface electronic states. We proceeded solving the anisotropic Eliashberg equations for increasing temperatures until the gaps vanished, yielding a critical temperature of CaB_2 of around 70 K. The picture for CaB_4 is overall quite similar, with some notable differences. Since the surface electronic state is absent in the tetraboride, its lowest gap is now only formed by the π electronic state, and thus is much less anisotropic [Fig. 3(e)]. At 5 K temperature, the highest gap value of CaB_4 (15.6 meV) is less strong than in CaB_2. Moreover, the two σ electronic sheets on the Fermi surface, which form the strongest gap in the diboride case, give rise to two slightly separated gaps in the tetraboride case (by less than 1 meV at 5 K). As compared to CaB_4, the slightly weaker gap energies of CaB_4 result in a lower critical temperature of 64 K.

Therefore, our anisotropic Eliashberg results clearly show that CaB_2 and CaB_4 host distinctly multigap superconductivity in combination with a notably high critical temperature. Here, it is worth noting that CaB_4 has the highest cohesive energy among the different configurations (thus, it is relatively more stable) and that there is a considerable energy difference with Ca_2B_2, which has a critical temperature of merely $\sim$1 K. The calculated α^2F and λ clearly exceed those of MgB_2 and MgB_4 [31,34]. As explained above, the higher density of states at the Fermi level in the Ca-based compounds contributes to this enhanced EPC and the resulting augmented critical temperatures. Previously, Choi *et al.* obtained a T_c of 48 K in bulk CaB_2 based on anisotropic Eliashberg calculations [29], which is almost 10 K higher than that of bulk MgB_2. Interestingly, the T_c of MgB_2 decreases in the monolayer limit, while our calculated T_c values of the 2D structures

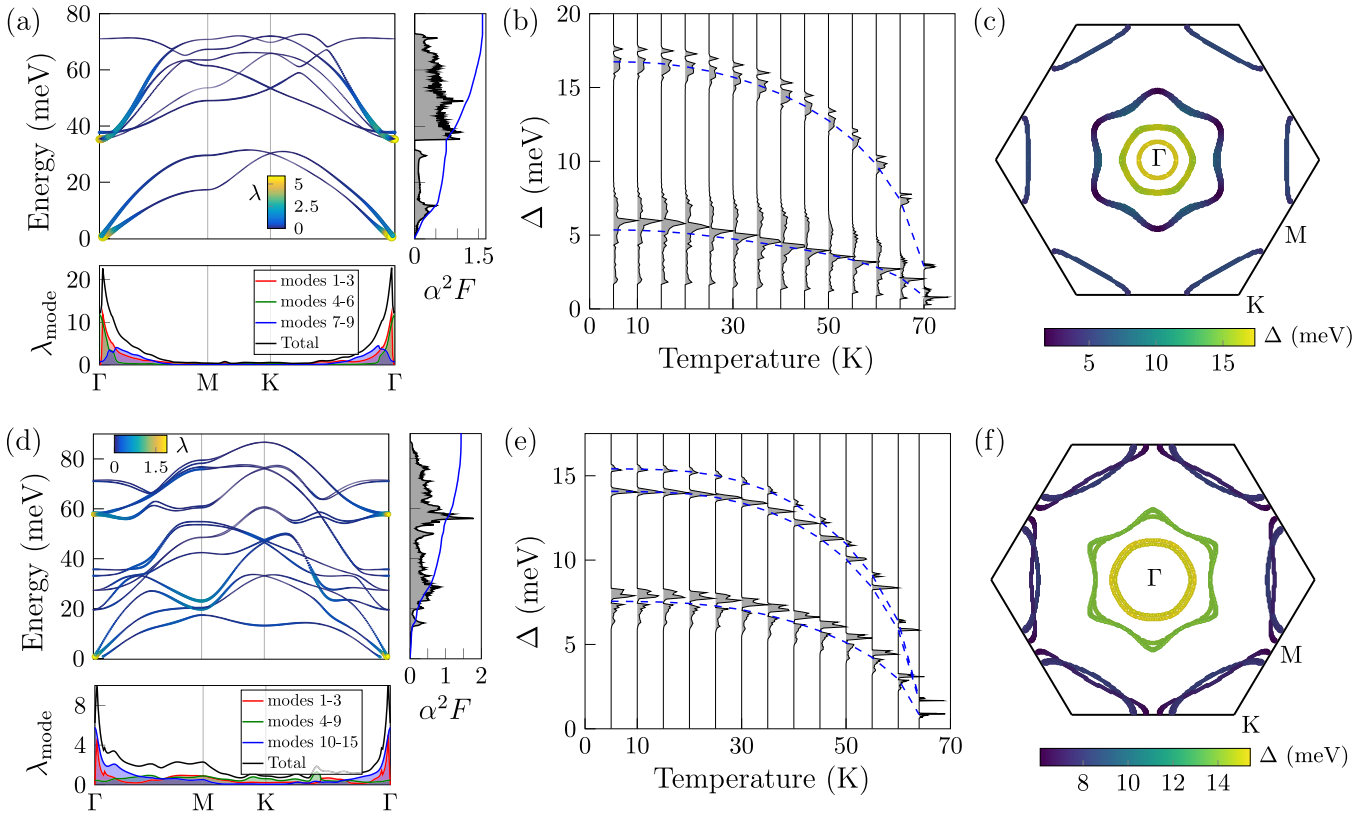

FIG. 3. Phonon dispersion with the mode-resolved electron-phonon coupling (EPC) indicated by colors and thickness, EPC λ_{mode} summed for three different groups of phonon modes, isotropic Eliashberg function α^2F, and EPC function λ for (a) CaB_2 and (d) CaB_4. Evolution of the superconducting gap distribution for (b) CaB_2 and (e) CaB_4. Momentum-dependent superconducting gap on the Fermi surface at 5 K for (c) CaB_2 and (f) CaB_4.

(CaB_2 as well as CaB_4) significantly exceed the bulk value obtained by Choi *et al.* [29].

Diborides of transition metals from group 5 of the periodic table—V, Nb, and Ta—also show promise to be good superconductors. Particularly, the critical temperature of NbB_2 in the isotropic limit is 35.5 K, which is three times higher than the isotropic value in monolayer MgB_2. However, for Nb and Ta diborides, we found that electronic smearing has a critical influence on phonons and EPC. With the standard electronic smearing value of 0.01 Ha, both structures show imaginary phonon frequencies in the vicinity of the *K* point, suggesting that the structures are not in their ground state. The unstable phonon mode, as shown in Fig. 4(h), is an acoustic mode with out-of-plane vibrations of Nb/Ta atoms.

By increasing the smearing value to 0.03 Ha, we managed to get rid of the imaginary phonon frequencies [Figs. 4(a) and 4(d)]. However, the instability transforms into a softening in the phonon dispersions of both compounds at the *K* point. These dips, as shown in Figs. 4(a) and 4(d), form EPC hot spots with the values of the coupling much higher compared to all other phonon modes. Thus, the total EPC and the critical temperature of NbB_2 and TaB_2 strongly depend on the electronic smearing used in the calculations. Therefore, the potential of these materials as superconductors may be impacted by the inclusion of phonon anharmonicity [61,62]. It is nevertheless interesting that both compounds, despite being quite close in their electronic and vibrational properties, show quite disparate superconducting behavior. The superconducting gap structure is more complex in transition-metal borides as compared to alkaline earth metal borides like MgB_2 and CaB_2. For NbB_2, this is mainly due to the outer semicircular sheet around the Γ point, shown in Fig. 4(c). The orbital character of this electronic sheet is not constant along the sheet because the character changes strongly at the points where the sheet shows indents. Namely, everywhere on this Fermi sheet, except for the indents, the electronic states mainly stem from the d_{z^2} orbital of Nb and p_z of B, which is similar to the states on the inner circular sheet around the Γ point [Fig. 4(g)]. These states from the two circular Fermi sheets form the strongest superconducting gap in NbB_2 [Fig. 4(b)]. All the remaining Fermi sheets together with the indent states of the outer sheet around Γ form the weakest, strongly anisotropic gap. Thus, in NbB_2, electronic states from one Fermi sheet contribute to two distinct superconducting gaps. TaB_2, calculated with the same parameters as NbB_2, shows very weak EPC compared to the former, and all the Fermi sheets form a single anisotropic gap [Figs. 4(e) and 4(f)].

The lightest transition metal of group 5, vanadium, forms a diboride structure without unstable phonons, even when calculated with the electronic smearing as low as 0.01 Ha [Fig. 5(a)]. Considering the out-of-plane nature of the unstable mode in both NbB_2 and TaB_2 [Fig. 4(h)], it appears that V, being lighter than its group neighbors, does not cause rippling of the structure, rendering it dynamically stable. Even though

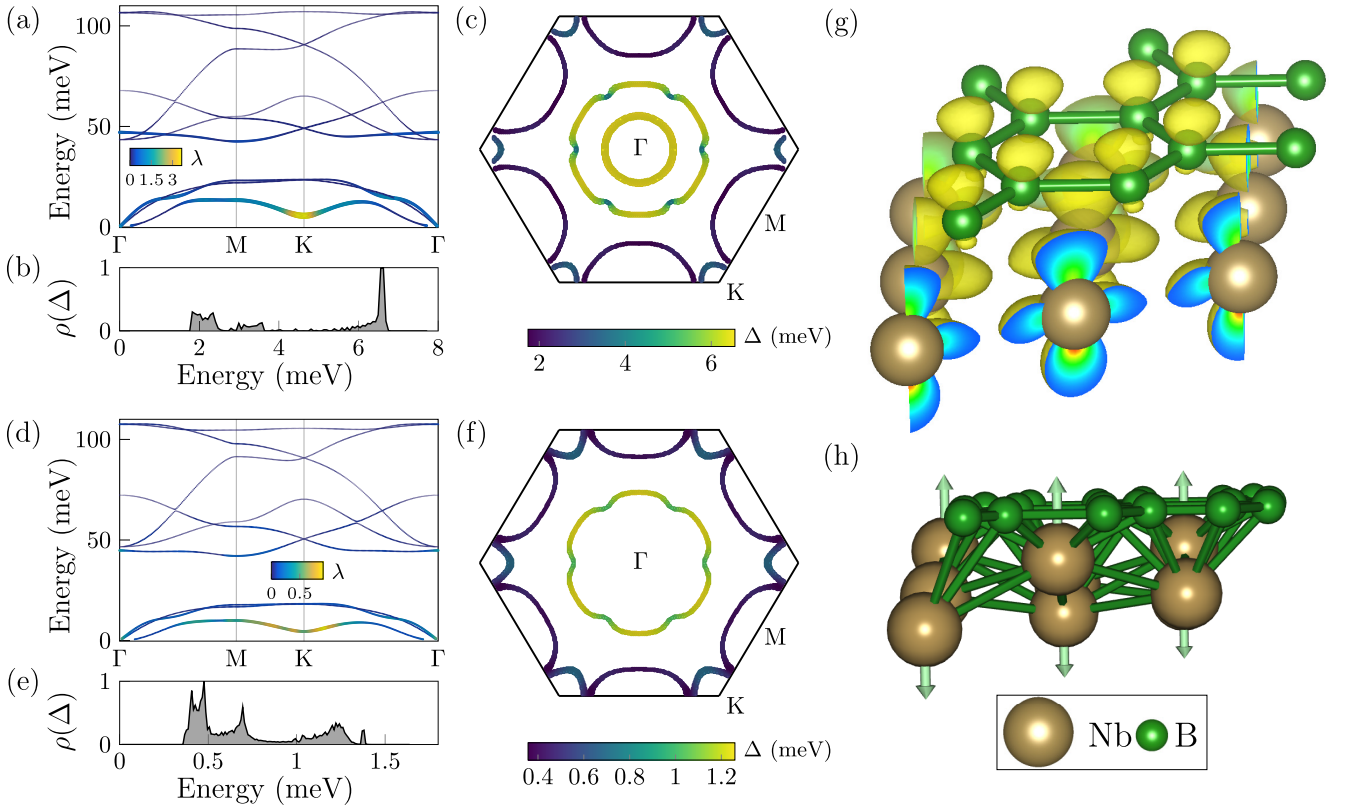

FIG. 4. Phonon dispersion with the mode-resolved electron-phonon coupling (EPC) indicated by colors and thickness for (a) NbB_2 and (d) TaB_2. Distribution of the superconducting gap of (b) NbB_2 at 5 K and (e) TaB_2 at 2 K. Momentum-dependent superconducting gap on the Fermi surface for (c) NbB_2 and at 5 K (f) TaB_2 at 2 K. (g) Norm of the wave function of the d_{z^2} state from the circular sheets around the Γ point of NbB_2. (h) Vibrational mode corresponding to the softening in the lowest acoustic phonon modes of NbB_2 and TaB_2.

V, Nb, and Ta belong to the same group, the Fermi surface of VB_2 [Fig. 5(b)] is quite different as compared to the diborides of Nb and Ta. In VB_2, there is no sheet around the *K* point and the two sheets around the Γ point have hexagonal and flowerlike shapes, respectively, in contrast to almost completely circular sheets in the two other diborides. The hexagonal sheet stems from a combination of out-of-plane *d* orbitals with considerable contribution of the d_{z^2} orbital, whereas the flower-shaped sheet is a mixture of in-plane and out-of-plane *d* orbitals of V without d_{z^2} contribution. VB_2 does share a common sheet with other diborides, namely, the circular sheet around the *M* point which corresponds to out-of-plane *d* orbitals of the *M* atom (d_{xz} and d_{yz}).

The total EPC for VB_2 is 1.13 with the main contributions coming from the acoustic phonon modes as well as the lowest optical mode corresponding to out-of-plane vibrations of boron atoms, as shown in Fig. 5(a). Interestingly, the superconducting gap on the Fermi surface shows the opposite pattern for VB_2 as compared to other MBenes of group 5. The electronic sheets around the Γ point, which are attributed

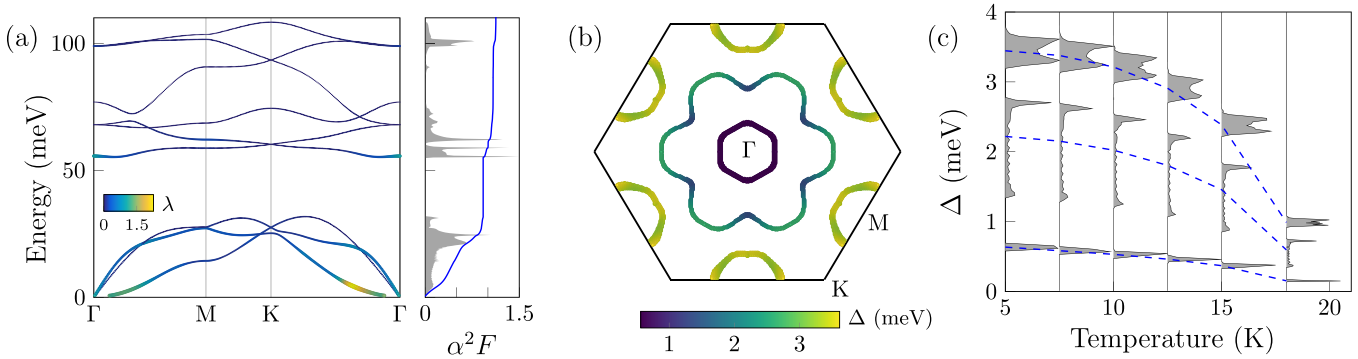

FIG. 5. Superconducting properties of VB_2: (a) Phonon dispersion with the mode-resolved electron-phonon coupling (EPC) indicated by colors and size. (b) Momentum-dependent superconducting gap on the Fermi surface. (c) Evolution of the superconducting gap distribution with temperature.

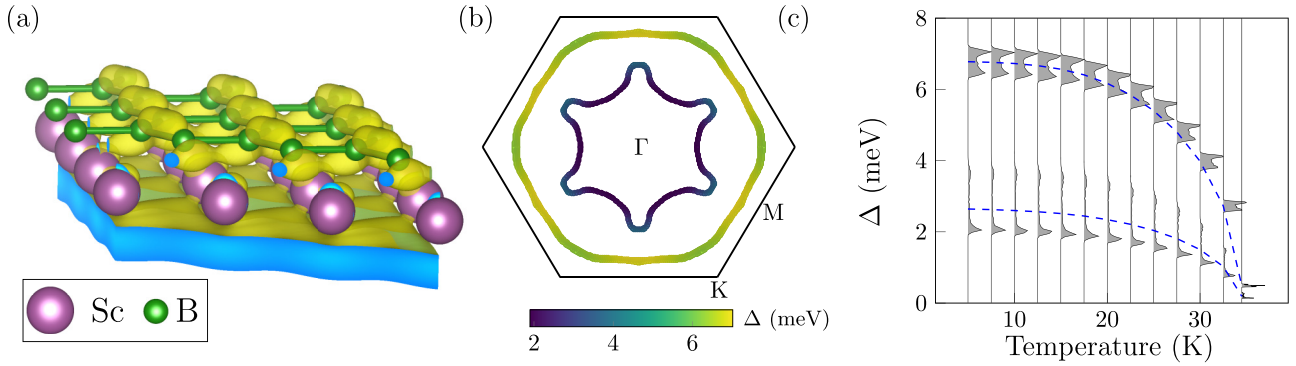

FIG. 6. (a) Surface electronic state of ScB_2, corresponding to the inner sheet of the Fermi surface. Superconducting properties of ScB_2, namely, (b) momentum-dependent superconducting gap on the Fermi surface and (c) evolution of the superconducting gap distribution with temperature.

mainly to the d_{z^2} orbital of the M atom, represent the strongest gap in both NbB_2 and TaB_2 [Figs. 4(c) and 4(f)]. In contrast, in VB_2 the Fermi sheet centered around Γ gives rise to the weakest gap, while the strongest gap appears around the M point. VB_2 has an additional gap of intermediate strength, stemming from the flower-shaped Fermi sheet around the Γ point. As a result, VB_2 is a three-gap superconductor. Our calculations show that the gaps vanish at the critical temperature of around 18.5 K.

The last material we have considered in more detail is ScB_2. Scandium belongs to group 3 of the periodic table, on the border between alkaline earth metals and transition metals. Since Sc has only one d electron in its outer shell, other electronic states can contribute more to the electronic states around the Fermi level. Therefore, ScB_2 represents an intermediate case between CaB_2 and the MBenes based on group-5 transition metals. The Fermi surface of ScB_2, shown in Fig. 6(b), consists of two sheets. The inner sheet corresponds to a surface state [Fig. 6(a)], akin to the one found in alkaline earth metal MBenes such as MgB_2 and CaB_2. However, in alkaline earth MBenes, the surface state stems from Mg/Ca-p states, whereas in ScB_2 it mainly has Sc-s character, because of scandium's different electronic configuration. The states of the outer sheet are a mixture of the boron p_z orbital and in-plane d orbitals of Sc. The total isotropic EPC of ScB_2 amounts to 1.27. Anisotropic Eliashberg calculation shows that ScB_2 is a two-gap superconductor [Fig. 6(b)], with the strongest gap stemming from the outer Fermi sheet and the weakest gap stemming from the inner sheet. The resulting critical temperature is rather high—around 34.5 K.

IV. CONCLUSION

Our systematic investigation performed with both isotropic and anisotropic Eliashberg theory calculations broadly sheds light on the potential of 2D metal-boride systems as superconducting materials. High critical temperatures (up to 72 K), as well as multigap superconducting behavior in CaB_2, CaB_4, VB_2, NbB_2, TaB_2, and ScB_2 structures were shown and detailed in this paper.

These results enable us to provide a general recipe for superconductivity in MBenes based on a boron honeycomb network. The key property here is the doping of the boron honeycomb network by the metal atoms. We obtained that the doping is optimal in MB_2 structures, leading to the highest DOS at the Fermi level (per atom) among all MBenes considered here. These high DOS instigate strong EPC, leading to 10 MB_2 compounds with sizable T_c's (see Table II), among which three cases outperform the prototype monolayer MB_2, namely, ScB_2, NbB_2, and CaB_2. Adding another M layer, which gives rise to the M_2B_2 structure, leads to overdoping of the boron honeycomb sheet and therefore a strong reduction of the DOS at the Fermi level, which severely limits the EPC. As a result, only two superconducting cases of the M_2B_2 structure were found (with Mg and Re as M), with very modest T_c's. On the other hand, adding another boron layer to the MB_2 structure, yielding MB_4, is less detrimental. Naturally, here the doping per boron layer goes down, but nevertheless five cases were obtained with sufficient DOS at the Fermi level to sustain superconductivity. These are a subset of the M atoms, determined as able to produce superconductivity in MB_2, all being nontransition metal elements. First, many transition metal-based MB_4 structures were found to be dynamically unstable (see Supplemental Material). Second, those that were dynamically stable simply host very limited EPC in the M-based acoustic phonon modes, which was found to be a major source of EPC in the nontransition metal cases.

Coupled with the advent of their fabrication [63,64], the variety of electronic structures and Fermi surface configurations, together with the demonstrated richness of superconducting behavior in 2D metal borides, recommend their versatility for further exploration in fundamental (multi)functional heterostructures, as well as potential device applications.

ACKNOWLEDGMENTS

This paper is supported by Research Foundation-Flanders (FWO-Vlaanderen), Special Research Funds of the University of Antwerp (TOPBOF), the Scientific and Technological Research Council of Turkey (TUBITAK) under Contract No. COST-118F187, and the Air Force Office of Scientific Research under Award No. FA9550-19-1-7048. Computational resources were provided by the High Performance

and Grid Computing Center (TRGrid e-Infrastructure) of TUBITAK ULAKBIM and by the VSC (Flemish Supercomputer Center), funded by the FWO and the Flemish Government—department EWI. The collaborative effort in this paper was supported by the EU COST Action No. CA16218 NANOCOHYBRI.

[1] X. Liu and M. C. Hersam, 2D materials for quantum information science, Nat. Rev. Mater. **4**, 669 (2019).

[2] C. Liu, H. Chen, S. Wang, Q. Liu, Y.-G. Jiang, D. W. Zhang, M. Liu, and P. Zhou, Two-dimensional materials for next-generation computing technologies, Nat. Nanotechnol. **15**, 545 (2020).

[3] D. Akinwande, C. Huyghebaert, C.-H. Wang, M. I. Serna, S. Goossens, L.-J. Li, H. S. P. Wong, and F. H. L. Koppens, Graphene and two-dimensional materials for silicon technology, Nature (London) **573**, 507 (2019).

[4] F. Schwierz, J. Pezoldt, and R. Granzner, Two-dimensional materials and their prospects in transistor electronics, Nanoscale **7**, 8261 (2015).

[5] C. Klinkert, Á. Szabó, C. Stieger, D. Campi, N. Marzari, and M. Luisier, 2-D materials for ultrascaled field-effect transistors: One hundred candidates under the ab initio microscope, ACS Nano **14**, 8605 (2020).

[6] F. R. Fan and W. Wu, Emerging devices based on two-dimensional monolayer materials for energy harvesting, Research **2019**, 7367828 (2019).

[7] M. B. Ghasemian, T. Daeneke, Z. Shahrbabaki, J. Yang, and K. Kalantar-Zadeh, Peculiar piezoelectricity of atomically thin planar structures, Nanoscale **12**, 2875 (2020).

[8] C. Sevik, D. Çakır, O. Gülseren, and F. M. Peeters, Peculiar piezoelectric properties of soft two-dimensional materials, J. Phys. Chem. C **120**, 13948 (2016).

[9] S. Sarıkurt, T. Kocabas, and C. Sevik, High-throughput computational screening of 2D materials for thermoelectrics, J. Mater. Chem. A **8**, 19674 (2020).

[10] Z. Meng, R. M. Stolz, L. Mendecki, and K. A. Mirica, Electrically-transduced chemical sensors based on two-dimensional nanomaterials, Chem. Rev. **119**, 478 (2019).

[11] J. Kou, E. P. Nguyen, A. Merkoçi, and Z. Guo, 2-dimensional materials-based electrical/optical platforms for smart on-off diagnostics applications, 2D Mater. **7**, 032001 (2020).

[12] E. Lee and D.-J. Kim, Review— recent exploration of two-dimensional MXenes for gas sensing: From a theoretical to an experimental view, J. Electrochem. Soc. **167**, 037515 (2020).

[13] S. Qin, J. Kim, Q. Niu, and C.-K. Shih, Superconductivity at the two-dimensional limit, Science **324**, 1314 (2009).

[14] T. Zhang, P. Cheng, W.-J. Li, Y.-J. Sun, G. Wang, X.-G. Zhu, K. He, L. Wang, X. Ma, X. Chen, Y. Wang, Y. Liu, H.-Q. Lin, J.-F. Jia, and Q.-K. Xue, Superconductivity in one-atomic-layer metal films grown on Si(111), Nat. Phys. **6**, 104 (2010).

[15] Y. Cao, A. Mishchenko, G. L. Yu, E. Khestanova, A. P. Rooney, E. Prestat, A. V. Kretinin, P. Blake, M. B. Shalom, C. Woods, J. Chapman, G. Balakrishnan, I. V. Grigorieva, K. S. Novoselov, B. A. Piot, M. Potemski, K. Watanabe, T. Taniguchi, S. J. Haigh, A. K. Geim *et al.*, Quality heterostructures from two-dimensional crystals unstable in air by their assembly in inert atmosphere, Nano Lett. **15**, 4914 (2015).

[16] M. M. Ugeda, A. J. Bradley, Y. Zhang, S. Onishi, Y. Chen, W. Ruan, C. Ojeda-Aristizabal, H. Ryu, M. T. Edmonds, H.-Z. Tsai, A. Riss, S.-K. Mo, D. Lee, A. Zettl, Z. Hussain, Z.-X. Shen, and M. F. Crommie, Characterization of collective ground states in single-layer $NbSe_2$, Nat. Phys. **12**, 92 (2016).

[17] J.-F. Ge, Z.-L. Liu, C. Liu, C.-L. Gao, D. Qian, Q.-K. Xue, Y. Liu, and J.-F. Jia, Superconductivity above 100 k in single-layer FeSe films on doped $SrTiO_3$, Nat. Mater. **14**, 285 (2015).

[18] S.-H. Cheng, Y. Zhang, H.-Z. Wang, Y.-L. Li, C. Yang, and Y. Wang, Fabrication and characterization of superconducting MgB_2 thin film on graphene, AIP Adv. **8**, 075015 (2018).

[19] C. Xu, L. Wang, Z. Liu, L. Chen, J. Guo, N. Kang, X.-L. Ma, H.-M. Cheng, and W. Ren, Large-area high-quality 2D ultrathin Mo_2 C superconducting crystals, Nat. Mater. **14**, 1135 (2015).

[20] V. Kamysbayev, A. S. Filatov, H. Hu, X. Rui, F. Lagunas, D. Wang, R. F. Klie, and D. V. Talapin, Covalent surface modifications and superconductivity of two-dimensional metal carbide MXenes, Science **369**, 979 (2020).

[21] G. Profeta, M. Calandra, and F. Mauri, Phonon-mediated superconductivity in graphene by lithium deposition, Nat. Phys. **8**, 131 (2012).

[22] D. M. Guzman, H. M. Alyahyaei, and R. A. Jishi, Superconductivity in graphene-lithium, 2D Mater. **1**, 021005 (2014).

[23] B. M. Ludbrook, G. Levy, P. Nigge, M. Zonno, M. Schneider, D. J. Dvorak, C. N. Veenstra, S. Zhdanovich, D. Wong, P. Dosanjh, C. Straßer, A. Stöhr, S. Forti, C. R. Ast, U. Starke, and A. Damascelli, Evidence for superconductivity in Li-decorated monolayer graphene, Proc. Natl. Acad. Sci. USA **112**, 11795 (2015).

[24] Y. Cao, V. Fatemi, S. Fang, K. Watanabe, T. Taniguchi, E. Kaxiras, and P. Jarillo-Herrero, Unconventional superconductivity in magic-angle graphene superlattices, Nature (London) **556**, 43 (2018).

[25] J. Nagamatsu, N. Nakagawa, T. Muranaka, Y. Zenitani, and J. Akimitsu, Superconductivity at 39 K in magnesium diboride, Nature (London) **410**, 63 (2001).

[26] V. A. Gasparov, N. S. Sidorov, I. I. Zver'kova, and M. P. Kulakov, Electron transport in diborides: Observation of superconductivity in ZrB_2, J. Exp. Theor. **73**, 532 (2001).

[27] L. Leyarovska and E. Leyarovski, A search for superconductivity below 1 K in transition metal borides, J. Less Common. Met. **67**, 249 (1979).

[28] H. Rosner, W. E. Pickett, S.-L. Drechsler, A. Handstein, G. Behr, G. Fuchs, K. Nenkov, K.-H. Müller, and H. Eschrig, Electronic structure and weak electron-phonon coupling in TaB_2, Phys. Rev. B **64**, 144516 (2001).

[29] H. J. Choi, S. G. Louie, and M. L. Cohen, Prediction of superconducting properties of cab_2 using anisotropic Eliashberg theory, Phys. Rev. B **80**, 064503 (2009).

[30] J. Bekaert, L. Bignardi, A. Aperis, P. van Abswoude, C. Mattevi, S. Gorovikov, L. Petaccia, A. Goldoni, B. Partoens, P. M. Oppeneer, F. M. Peeters, M. V. Milošević, P. Rudolf, and C. Cepek, Free surfaces recast superconductivity in few-monolayer MgB_2: Combined first-principles and ARPES demonstration, Sci. Rep. **7**, 14458 (2017).

[31] J. Bekaert, A. Aperis, B. Partoens, P. M. Oppeneer, and M. V. Milošević, Evolution of multigap superconductivity in the atomically thin limit: Strain-enhanced three-gap superconductivity in monolayer MgB_2, Phys. Rev. B **96**, 094510 (2017).

[32] J. Bekaert, M. Petrov, A. Aperis, P. M. Oppeneer, and M. V. Milošević, Hydrogen-Induced High-Temperature Superconductivity in Two-Dimensional Materials: The Example of Hydrogenated Monolayer MgB_2, Phys. Rev. Lett. **123**, 077001 (2019).

[33] Y. Zhao, C. Lian, S. Zeng, Z. Dai, S. Meng, and J. Ni, Two-gap and three-gap superconductivity in AlB_2-based films, Phys. Rev. B **100**, 094516 (2019).

[34] Y. Zhao, C. Lian, S. Zeng, Z. Dai, S. Meng, and J. Ni, MgB_4 trilayer film: A four-gap superconductor, Phys. Rev. B **101**, 104507 (2020).

[35] G. Akopov, M. T. Yeung, and R. B. Kaner, Rediscovering the crystal chemistry of borides, Adv. Mater. **29**, 1604506 (2017).

[36] M. Khazaei, J. Wang, M. Estili, A. Ranjbar, S. Suehara, M. Arai, K. Esfarjani, and S. Yunoki, Novel MAB phases and insights into their exfoliation into 2D MBenes, Nanoscale **11**, 11305 (2019).

[37] Y. Gogotsi and B. Anasori, The rise of MXenes, ACS Nano **13**, 8491 (2019).

[38] See Supplemental Material at http://link.aps.org/supplemental/10.1103/PhysRevMaterials.6.024803 for the structural, energetic, electronic, vibrational, and superconducting properties of all the considered materials.

[39] X. Gonze, B. Amadon, G. Antonius, F. Arnardi, L. Baguet, J.-M. Beuken, J. Bieder, F. Bottin, J. Bouchet, E. Bousquet, N. Brouwer, F. Bruneval, G. Brunin, T. Cavignac, J.-B. Charraud, W. Chen, M. Côté, S. Cottenier, J. Denier, G. Geneste *et al.*, The Abinit project: Impact, environment and recent developments, Comput. Phys. Commun. **248**, 107042 (2020).

[40] X. Gonze, F. Jollet, F. Abreu Araujo, D. Adams, B. Amadon, T. Applencourt, C. Audouze, J.-M. Beuken, J. Bieder, A. Bokhanchuk, E. Bousquet, F. Bruneval, D. Caliste, M. Côté, F. Dahm, F. Da Pieve, M. Delaveau, M. Di Gennaro, B. Dorado, C. Espejo *et al.*, Recent developments in the ABINIT software package, Comput. Phys. Commun. **205**, 106 (2016).

[41] M. van Setten, M. Giantomassi, E. Bousquet, M. Verstraete, D. Hamann, X. Gonze, and G.-M. Rignanese, The PseudoDojo: Training and grading a 85 element optimized norm-conserving pseudopotential table, Comput. Phys. Commun. **226**, 39 (2018).

[42] S. Y. Savrasov and D. Y. Savrasov, Electron-phonon interactions and related physical properties of metals from linear-response theory, Phys. Rev. B **54**, 16487 (1996).

[43] G. M. Eliashberg, Interactions between electrons and lattice vibrations in a superconductor, J. Exp. Theor. **11**, 696 (1960).

[44] G. M. Eliashberg, Temperature Green's function for electrons in a superconductor, J. Exp. Theor. **12**, 1000 (1961).

[45] F. Giustino, Electron-phonon interactions from first principles, Rev. Mod. Phys. **89**, 015003 (2017).

[46] W. L. McMillan, Transition temperature of strong-coupled superconductors, Phys. Rev. **167**, 331 (1968).

[47] P. B. Allen and R. C. Dynes, Transition temperature of strong-coupled superconductors reanalyzed, Phys. Rev. B **12**, 905 (1975).

[48] P. B. Allen and B. Mitrović, Theory of superconducting T_c, Solid State Phys. **37**, 1 (1983).

[49] G. Grimvall, *The Electron-Phonon Interaction* (North Holland Publishing Co., Amsterdam, 1981)

[50] F. Giustino, M. L. Cohen, and S. G. Louie, Electron-phonon interaction using Wannier functions, Phys. Rev. B **76**, 165108 (2007).

[51] J. Noffsinger, F. Giustino, B. D. Malone, C.-H. Park, S. G. Louie, and M. L. Cohen, EPW: A program for calculating the electron-phonon coupling using maximally localized Wannier functions, Comput. Phys. Commun. **181**, 2140 (2010).

[52] P. Giannozzi, S. Baroni, N. Bonini, M. Calandra, R. Car, C. Cavazzoni, D. Ceresoli, G. L. Chiarotti, M. Cococcioni, I. Dabo, A. D. Corso, S. de Gironcoli, S. Fabris, G. Fratesi, R. Gebauer, U. Gerstmann, C. Gougoussis, A. Kokalj, M. Lazzeri, L. Martin-Samos *et al.*, QUANTUM ESPRESSO: A modular and open-source software project for quantum simulations of materials, J. Phys.: Condens. Matter **21**, 395502 (2009).

[53] M. Methfessel and A. T. Paxton, High-precision sampling for Brillouin-zone integration in metals, Phys. Rev. B **40**, 3616 (1989).

[54] S. Baroni, S. de Gironcoli, A. Dal Corso, and P. Giannozzi, Phonons and related crystal properties from density-functional perturbation theory, Rev. Mod. Phys. **73**, 515 (2001).

[55] E. R. Margine and F. Giustino, Anisotropic Migdal-Eliashberg theory using Wannier functions, Phys. Rev. B **87**, 024505 (2013).

[56] A. A. Mostofi, J. R. Yates, Y.-S. Lee, I. Souza, D. Vanderbilt, and N. Marzari, wannier90: A tool for obtaining maximally-localised Wannier functions, Comput. Phys. Commun. **178**, 685 (2008).

[57] T. Aizawa, W. Hayami, and S. Otani, Surface phonon dispersion of $ZrB_2(0001)$ and $NbB_2(0001)$, Phys. Rev. B **65**, 024303 (2001).

[58] C. Zhang, T. He, S. K. Matta, T. Liao, L. Kou, Z. Chen, and A. Du, Predicting novel 2D MB_2 (M = Ti, Hf, V, Nb, Ta) monolayers with ultrafast Dirac transport channel and electron-orbital controlled negative Poisson's ratio, J. Phys. Chem. **10**, 2567 (2019).

[59] J.-H. Liao, Y.-C. Zhao, Y.-J. Zhao, H. Xu, and X.-B. Yang, Phonon-mediated superconductivity in Mg intercalated bilayer borophenes, Phys. Chem. Chem. Phys. **19**, 29237 (2017).

[60] J. M. An and W. E. Pickett, Superconductivity of MB_2: Covalent Bonds Driven Metallic, Phys. Rev. Lett. **86**, 4366 (2001).

[61] A. Y. Liu, I. I. Mazin, and J. Kortus, Beyond Eliashberg Superconductivity in MgB_2: Anharmonicity, Two-Phonon Scattering, and Multiple Gaps, Phys. Rev. Lett. **87**, 087005 (2001).

[62] H. J. Choi, D. Roundy, H. Sun, M. L. Cohen, and S. G. Louie, First-principles calculation of the superconducting transition in MgB_2 within the anisotropic Eliashberg formalism, Phys. Rev. B **66**, 020513(R) (2002).

[63] X. Hu, S. Guo, S. Zhang, X. Guo, Y. Li, S. Huang, K. Zhang, and J. Zhu, Two-dimensional transition metal diborides: Promising Dirac electrocatalysts with large reaction regions toward efficient N_2 fixation, J. Mater. Chem. A **7**, 25887 (2019).

[64] H. Yang and L. Chu, MBenes: Two-dimensional transition-metal borides with ordered metal vacancies, Chin. Chem. Lett. (2021), doi: 10.1016/j.cclet.2021.10.078.